ARTICLE

Tailored MXene-derived Nano-Heterostructure Oxide for Peroxymonosulfate Activation in the Treatment of Municipal Wastewaters

Received 00th January 20xx,
Accepted 00th January 20xx

DOI: 10.1039/x0xx00000x

Shalu Atri,[a,b*], Elham Loni,[b] Zuzana Dyrcikova,[c] Frantisek Zazimal,[d] Maria Caplovicova,[e] Dana Dvoranova,[c] Gustav Plesch,[a] Miroslava Kabatova,[f] Marcello Brigante,[g] Michael Naguib,[b,h*] Olivier Monfort[i*]

Nowadays, in the field of environmental protection, a huge effort is focused on efficient and sustainable processes to treat wastewaters. The current study emphasizes the photocatalytic performance of $TiNbO_x$, a nano-heterostructure material derived from the oxidation of $(Ti_{0.75}Nb_{0.25})_2CT_x$ MXene. $TiNbO_x$ nano-heterostructure exhibited remarkable performance in the degradation of caffeine (CAF) and sulfamethoxazole (SMX) under UVA irradiation in the presence of peroxymonosulfate (PMS). Under optimal conditions, 0.2 g L^{-1} of $TiNbO_x$, 0.5 mM PMS and 50 µM concentration of pollutants, and natural pH of deionized water, we observed a complete degradation of SMX and 91 % degradation of CAF. Scavenging studies provided evidence for the involvement of $^{\bullet}OH$ and $SO_4^{\bullet-}$ in the degradation of the pollutants, which was also supported by indirect techniques of electron paramagnetic resonance (EPR) spectroscopy. The degradation pathway of the pollutants was analyzed by liquid chromatography-mass spectrometry (LC-MS) and suggested several mechanisms including hydroxylation and isoxazole ring-opening reactions. In addition, X-ray photoelectron spectroscopy (XPS) supported the proposed degradation mechanism. The reusability test underscored the high stability and efficiency of $TiNbO_x$. Moreover, the significance of this research was emphasized by conducting degradation studies in tap water (TW) and tertiary effluents of the wastewater (WW) treatment plant in Bratislava. Under optimal conditions, 49 % and 30 % of CAF were degraded in TW and WW, respectively, after 12 hours of reaction. For SMX, 68 % and 67 % degradation were obtained in TW and WW, respectively.

Introduction

The products of our daily lives, such as personal care products, pharmaceutically active compounds and drugs like antibiotics, analgesics, anti-inflammatories, and antiepileptics, etc., have been considered as contaminants of emerging concern (CEC).[1] CECs can be described as pollutants that are detected in the environmental monitoring sample and have adverse effects on aquatic life and its ecosystem, as well as human life through their bioaccumulation process.[2] Sulfamethoxazole (SMX) is a widely used antibiotic, and it is one of the main sources of pollution in wastewater of pharmaceutical companies and conventional wastewater treatment plants.[3] Caffeine (CAF) is another highly consumed substance around the world from medicines, coffee, and illicit drugs.[1] After ingestion, this CAF is partially metabolized and then excreted by the body, contaminating wastewater.[4] Existing conventional methods cannot completely remove these pollutants from the wastewater, leading to their accumulation in the natural environment, which poses a serious public health issue.[5] Although CAF lacks specific regulatory limits, while SMX is regulated with a maximum allowable concentration of 0.1 µg/L in surface waters in the EU. Thereby both compounds require careful consideration of their degradation products during treatment evaluations.

Advanced oxidation processes (AOPs) are among the most promising treatment methods to remove water pollution as they can completely degrade organic pollutants into CO_2, H_2O, and inorganic ions.[6] In AOPs, hydroxyl radicals ($^{\bullet}OH$) are generated by photocatalytic and Fenton-based processes. These hydroxyl radicals are strong and non-selective oxidants.[6] Having stronger oxidation

[a.] Department of Inorganic Chemistry, Faculty of Natural Sciences, Comenius University Bratislava, Ilkovicova 6, Mlynska Dolina, SK-842 15 Bratislava, Slovak Republic
[b.] Department of Physics and Engineering Physics, Tulane University, New Orleans, Louisiana 70118, United States of America
[c.] Institute of Physical Chemistry and Chemical Physics, Faculty of Chemical and Food Technology, Slovak University of Technology in Bratislava, Radlinskeho 9, SK-812 37 Bratislava, Slovak Republic
[d.] Department of Plasma Physics and Technology, Faculty of Science, Masaryk University, Kotlarska 267/2, 611 37 Brno, CZ-602 00, Czech Republic
[e.] STU Center for Nanodiagnostics, Faculty of Materials Science and Technology in Trnava, Slovak Technical University in Bratislava, Vazovova 5, 81243 Bratislava, Slovak Republic
[f.] Bratislavská vodárenská spoločnosť a.s., Prešovská 48, 826 46 Bratislava, Slovak Republic
[g.] Université Clermont Auvergne, CNRS, Institut de Chimie de Clermont-Ferrand, Clermont-Ferrand, F-63000, France
[h.] Department of Chemistry, Tulane University, New Orleans, Louisiana 70118, United States of America
[i.] Centre for Nanotechnology and Advanced Materials, Faculty of Mathematics Physics and Informatics, Comenius University Bratislava, Mlynska Dolina, SK-842 48 Bratislava, Slovak Republic
*Corresponding authors: shalu1@uniba.sk (SA); naguib@tulane.edu (MN); olivier.monfort@uniba.sk (OM)
† Footnotes relating to the title and/or authors should appear here.
Supplementary Information available: DRS, FTIR, Degradation curve for caffeine degradation by varying pH, Catalyst dosage and PMS concentration, XPS spectra before and after CAF/SMX degradation, TOC bar graph

capacity, higher selectivity for aromatic organic compounds, and greater stability in a wide pH range makes sulfate radicals ($SO_4^{\bullet-}$) more promising than $^{\bullet}OH$.[7, 8] The $SO_4^{\bullet-}$ can be generated by the cleavage of peroxydisulfate (PDS) and peroxymonosulfate (PMS) in the presence of light, heating, transition, and alkaline earth metals.[9] However, these activation processes cannot be yet scaled up, as some of the transition metals might have a toxic nature, might be unstable at natural pH, or consume too much energy.[10] To address these issues, heterogeneous catalysts have been found to efficiently activate PMS/PDS oxidants.[11, 12] Therefore, research based on heterogeneous AOPs is currently a hot area of research to solve some of the environmental issues.

As heterogeneous catalysts, 2D layered materials are promising candidates due to their high specific surface area, large number of surface-active sites, and superior electron mobility, which minimizes the recombination of charge carriers.[13] In the past few years, atomically thin 2D multilayered transition metal carbides and nitrides, known as MXenes, have emerged as cocatalysts because of their unique structure and electronic conductivities, as well as ability to tailor the functionalities present on their surface.[14-17]The functional groups associated with MXenes (e.g., $Ti_3C_2T_x$ and Ti_2CT_x, T_x stands for surface terminations) bestowed the formation of MXene-derived metal oxides (MO_x), MO_x/MXene, and MO_x/carbon/MXene heterojunction materials by a mild, partial, and full oxidation process.[18-22] The beauty of utilizing MXene as the precursor to attain MO_x is that it provides a unique morphology and physiochemical properties that cannot be accessed by other synthetic routes.[22, 23] Several studies have already demonstrated the excellent performance of different catalysts to activate PDS and PMS into $^{\bullet}OH$, $SO_4^{\bullet-}$ and $^1O_2$.[12] However, few of these studies take a comprehensive approach, and many lack a detailed explanation for the activation process.[24-26]

In this context, this study aims to investigate the role of a new type of catalyst, $TiNbO_x$ derived from Nb-substituted Ti_2CT_x MXene, in PMS activation for the degradations of both CAF and SMX. The photoinduced activation of PMS by $TiNbO_x$ is explored for the first time in tertiary effluents from a wastewater treatment plant (WWTP) in Bratislava-Petrzalka. This study discusses the effect of reaction conditions such as pH, catalyst, and PMS concentrations on the degradation of CAF and SMX. The identified reactive oxygen species (ROS) and the proposed degradation pathway were determined by electron paramagnetic resonance (EPR), X-ray photoelectron spectroscopy (XPS), and liquid chromatography-mass spectrometry (LC-MS).

Results and discussion

MXenes are not considered as photocatalysts but they can be used as cocatalysts. However, the oxidation of MXenes can act as efficient photocatalyst by combining the properties of both MXene precursor and the resulting oxide, thus offering potential unique photocatalytic properties.[27] In the current study, we aimed to prepare innovative oxide nano-heterostructures ($TiNbO_x$) derived from oxidation of $(Ti_yNb_{1-y})_2CT_x$ MXene that retains the layered morphological features of the MXene precursors as drawn in scheme 1. The resulting $TiNbO_x$ can activate PMS for degradation of CECs, thus being potentially employed as additive treatment in municipal wastewaters treatment plants.

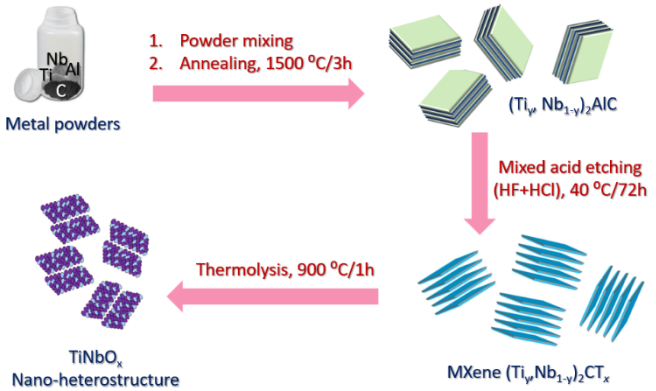

Scheme 1 Schematic representation of preparation of $TiNbO_x$ oxide nano-heterostructure.

Materials structural, morphological, and optical properties

Fig. 1 shows the XRD patterns for Nb-substituted MAX referred to with the formula $(Ti_{0.75}Nb_{0.25})_2AlC$, and its corresponding MXene, $(Ti_{0.75}Nb_{0.25})_2CT_x$, obtained by HF etching. The XRD pattern for the MAX phase agrees with the reported literature.[22, 28] Compared to MAX, the XRD pattern of the MXene shows a significant shift in *002* reflection towards a lower angle and the disappearance of mixed *hkl* reflections, suggesting the extraction of the Al layers and the enlargement of interlayer spacing due to surface functionalization (Fig. 1a).[14, 22] Furthermore, the morphology of the MAX phase and MXene was analyzed by SEM (Fig. S1a and S1b) (ESI†), which confirmed the successful etching of the Al layers and the formation of MXene, as the accordion morphology can be clearly noticed in Fig. S1b (ESI†). The as-prepared MXene was subjected to oxidation, to get a fully Nb-substituted titanium oxide ($TiNbO_x$) material. The XRD pattern after oxidation (Fig. 1a) suggests the formation of a biphasic oxide compound. The marked reflections at 2θ of 27.39°, 36.03°, 41.19°, 44.13°, 54.32°, 56.74°, and 62.76° correspond to rutile TiO_2 as major phase, while the rest of the reflections are analogous to $Ti_2Nb_{10}O_{29}$ in monoclinic symmetry (Fig. 1a). The SEM image in Fig. S1c (ESI†) highlights the oxidation of MXene nanosheets, resulting in oxide particles smaller than 5µm composed of aggregated nanosheets. Based on EDS analysis, the stoichiometric ratio between Ti and Nb remained consistent from the MXene precursors to the TiNbOx product, with a significant amount of carbon still present (Table S1).

The nanostructure of the sample was further investigated by TEM, HRTEM, STEM, and EFTEM-SI methods. Low magnification SE-STEM image, Fig. 1b, shows that the sample consists of nanostructures showing a sheet morphology, which were formed by the fusion of nanocrystals from 50 nm to 70 nm in size. More detailed image depicting a portion of the nanosheet where nanocrystals are fused is in Fig. 1c. EFTEM -SI mapping showed uneven distribution of Ti (generated by Ti-$L_{2,3}$ edge), Nb (generated by Nb-M edge), and O (generated by O-K edge) elements throughout the nanosheets. This is manifested in RGB composite image, Fig. 1d, generated by superposition of Ti (green) and Nb (blue) elemental maps. Fig. 1d

indicates that nanosheets are heterostructures consisted of fused titania TiO_2 (Ti: 32,6 at %, O: 67.4 at%) and $Ti_2Nb_{10}O_{29}$ (Ti: 8.0 at%, Nb: 23.9 at%, 68.1 at%) nanoparticles. HRTEM method was used to determine TiO_2 polymorph in nanosheets. By evaluation of FFT pattern, Fig. 1f, recorded from highlighted area in Fig. 1e it was determined that nanoparticle is rutile TiO_2 single crystal oriented along [$1\bar{1}1$] direction. This is in accordance with result obtained by XRD method, Fig.1a. HRTEM method was used to confirms the presence of $Ti_2Nb_{10}O_{29}$ in nanosheets, as manifested in Figs. 1g, h. Figs. 1g, h also shows that $Ti_2Nb_{10}O_{29}$ nanocrystal with a monoclinic crystal structure is surrounded by rutile TiO_2 (R) nanocrystals sharing the same interfaces, which proves the appearance of nano-heterostructures in the sample.[29] Based on this results it can be excluded a mixture of TiO_2 and $Ti_2Nb_{10}O_{29}$ nanoparticles in the sample or single-phase composition of the sample generated by incorporation of Nb atoms into structure of TiO_2. The TEM images show a nanoparticulate material that has retained the nanosheet-like morphology of its precursors, thereby providing higher specific surface area. Moreover, in $TiNbO_x$, nano-heterostructure with the highest proportion of rutile TiO_2 was accompanied by {101} and {110} types of planes (Fig. 1**e** and 1**f**), suggesting high photocatalytic activity.[30]

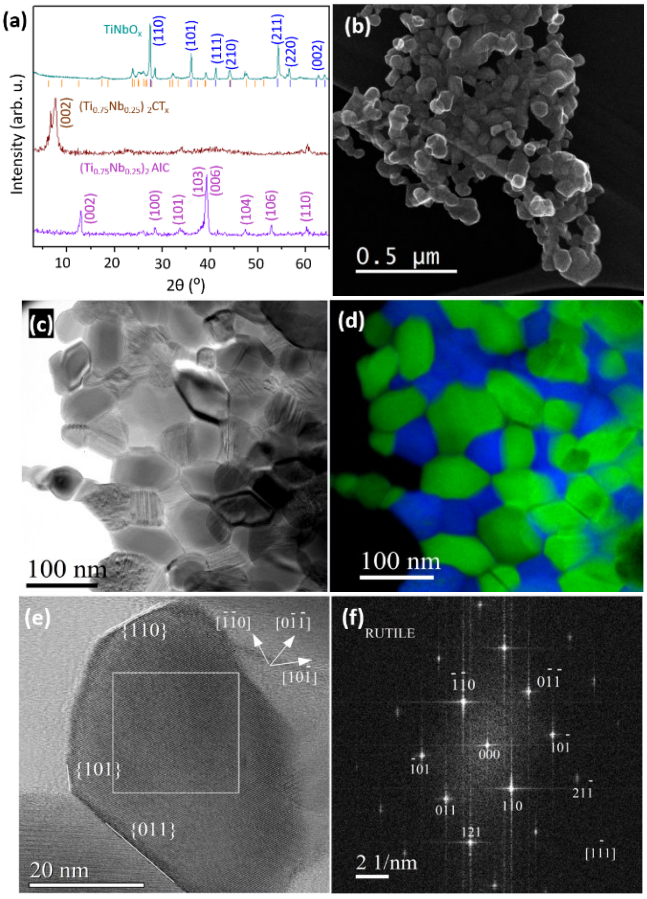

Fig 1 (a) XRD patterns of $(Ti_{0.75}Nb_{0.25})_2AlC$ (MAX), $(Ti_{0.75}Nb_{0.25})_2CT_x$ (MXene) and $TiNbO_x$. In the XRD pattern, the blue and orange lines correspond to rutile TiO_2 (PDF#00-001-1292) and monoclinic $Ti_2Nb_{10}O_{29}$ (PDF#00-040-0039), respectively. (b) low magnification SE STEM image of $TiNbO_x$ nanosheet. (c)TEM of nanosheet consisted of fused nanoparticles. (d) RGB Composite Ti (green) and Nb (blue) elemental maps indicating distribution of TiO_2 and $Ti_2Nb_{10}O_{29}$ grains in nanosheet. (e)HRTEM of rutile nanocrystal oriented along [$1\bar{1}1$] direction along with surface planes marked and (f) relevant FFT image acquired from highlighted area. (g) HRTEM image of nanosheet showing coexistence of rutile and $Ti_2Nb_{10}O_{29}$ nanocrystal oriented along [$2\bar{1}1$] direction. (h)FFT pattern acquired from squared area in (g).

Table 1 Characteristic parameters for $TiNbO_x$ obtained from BET analysis.

Sample identification	a [m^2/g]	b [cm^3g^{-1}]	c [cm^3g^{-1}]	d [cm^3g^{-1}]	e [cm^3g^{-1}]	F
$TiNbO_x$	+4	+1,0	0.014	0.001	0.021	little ME, less MI, more MA

a – specific surface area according to BET[31] - marked+; b – volume of the adsorbed monomolecular layer; c – cumulative pore volume according to Gurvich[32]; d – the cumulative volume of micropores (MI) according to Horvath-Kawazoe[33]; e – cumulative volume of mesopore (ME) and macropore (MA) according to BJH method[34, 35]; f – nature of the material.

In BET analysis, the multiscale porosity behavior of $TiNbO_x$ was observed with a specific surface area of 4 m^2g^{-1}, which is much lower than other reports for rutile TiO_2 nanoparticles (46.3 m^2g^{-1})[36] and slightly higher than $Ti_2Nb_{10}O_{29}$ (3.4 m^2g^{-1}) reported in the literature.[37] The smaller specific surface area for $TiNbO_x$ can be attributed to the strong fusion of TiO_2 and $Ti_2Nb_{10}O_{29}$ nanoparticles during the oxidation of MXene at high temperature (Fig. 1 and S1, ESI†), that arises from surface self-diffusion phenomenon.[38] The volume of mesopores is 0.021 cm^3g^{-1} which is 21 times higher than that of micropores, whereas the total volume of macropores is 0.167 cm^3g^{-1} (Table 1). Overall, $TiNbO_x$ has a predominantly low mesoporous (5-10, 10-50 nm) character with some very low micropore (3-5 nm) abundance but mainly more macropores (50-200, 200-300, 300-1000 nm).

Fig. S2 (ESI†) shows the UV-visible DRS spectra of the $TiNbO_x$. Assuming an indirect energy band gap (E_g) for plotting the Tauc's plots,[39] the estimated E_g is 2.87 eV (~ 432 nm) (Fig. S2b) (ESI†). Compared to reported values of E_g around 3.03 eV for rutile TiO_2[40] and 2.98 eV for monoclinic $Ti_2Nb_{10}O_{29}$[41], $TiNbO_x$ nano-heterostructure oxide derived from Nb substituted MXene possess a narrow band gap (2.87 eV), enabling better activation by solar light, though primarily by its UVA part. For this reason, the photoinduced experiments in this work were performed under UVA irradiation.

Effects of reaction conditions on the degradation of CAF and SMX

Fig. 2 displays the kinetic curves and apparent rate constants of CAF and SMX degradation by using 0.2 g L^{-1} of $TiNbO_x$ as a catalyst to activate PMS in the dark and under UVA light in aerated aqueous systems. In the dark, $TiNbO_x$ exhibited negligible effect on the

removal of both the pollutants via adsorption process (Fig. 2). CAF was not oxidized by PMS alone, while SMX was degraded by about 30 % either in the dark or under UVA irradiation (Fig. 2). Additionally, the photocatalysis with $TiNbO_x$ without the addition of PMS, resulted in the degradation of 47 % of CAF and 83 % of SMX (Fig. 2). Considering the above results, it is reasonable to conclude that photochemical activation of PMS for CAF and SMX degradation is negligible.

When $TiNbO_x$ was added to the systems containing PMS, a significant degradation of the pollutants is obtained in the dark, that was strongly enhanced under UVA, thus reaching 100 % for SMX (k' = 0.0314 min^{-1}) and 93% for CAF (k' = 0.0266 min^{-1}) after 2 h of reaction. The mineralization of CAF and SMX estimated by TOC (Fig. S3) (ESI†) was 69 % (k' = 0.0089 min^{-1}) and 60 % (k' = 0.0072 min^{-1}), respectively, after 2h of irradiation in the presence of 0.5 mM of PMS and 0.2 g L^{-1} of $TiNbO_x$. An incomplete mineralization of CAF and SMX signified that there might be presence of several degradation by-products, from which their identification will help in the determination of the degradation pathway (see section 3.5).
These results indicated that $TiNbO_x$ plays a crucial role in the activation of PMS that prompts to achievement of faster and more efficient degradation of both pollutants under UVA light. For CAF degradation, the kinetic graphs in Fig. 2c demonstrated a higher value of rate constants for $k'_{UVA+TiNbOx+PMS}$ which is 6 times of $k_{UVA+TiNbOx}$ and 12 times of $k'_{dark+TiNbOx+PMSt}$. Similarly, for SMX degradation, $k'_{UVA+TiNbOx+PMS}$ was found to be 2.3 times of $k'_{UVA+TiNbOx}$ and 6 times of $k'_{dark+TiNbOx+PMS}$ (Fig. 2d).

This observation confirmed a synergic effect between $TiNbO_x$ and PMS both in the dark and under UVA irradiation for the degradation of the pollutants. The synergic efficiency (SE) can be calculated by using the following eqns.1 and 2:

$$SE(UVA)=\frac{k'_{(UVA+TiNbOx+PMS)}}{k'_{(UVA)}+k'_{(TiNbOx)}+k'_{(PMS)}} \quad (1)$$

$$SE(dark)=\frac{k'_{(TiNbOx+PMS)}}{k'_{(TiNbOx)}+k'_{(PMS)}} \quad (2)$$

where, $k'_{UVA+TiNbOx+PMS}$, $k'_{TiNbOx+PMS}$, k'_{UVA}, k'_{PMS}, k'_{TiNbOx}, are the rate constants for CAF and SMX degradation for the systems referred in the subscripts.

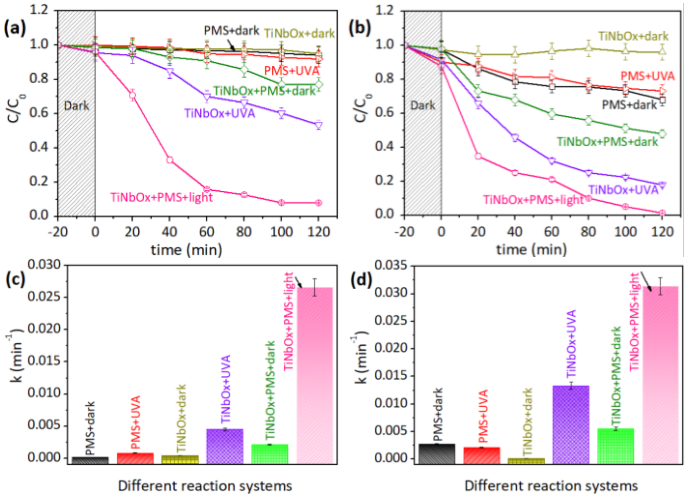

Fig. 2 Degradation data for (a) CAF and (b) SMX in various reaction systems, (c) CAF and (d) SMX degradation constant in PMS systems in dark and upon UVA exposure. Initial conditions: c_0(CAF) = c_0(SMX) = 50 µM, c_0(PMS) = 0.5 mM, c($TiNbO_x$) = 0.2 g L^{-1} at natural pH of distilled water.

The SE value for CAF degradation was derived to be 3.9 (dark) and 48.1 (UVA), whereas for SMX degradation was calculated to be 2.0 (dark) and 2.2 (UVA), respectively. The differences in SE values for SMX and CAF degradation can be attributed to their different molecular structure which impacts their adsorption on the catalyst. In addition, the structure of CAF might be more susceptible to the attack by ROS than SMX, thus explaining the larger difference in SE between dark and light, compared to SMX. So far, the observed higher photocatalytic activity of SMX than CAF is relevant to the literature since SMX is susceptible to photodegradation whereas CAF exhibits conservative photoreactivity.[42]

To further explore the effect of reaction conditions on the degradation of the pollutants, several parameters such as $TiNbO_x$ dosage, PMS concentration, and pH variation were only investigated and discussed for CAF degradation (Text S1 and Fig. S4 and S5) (ESI†). Indeed, this system exhibits a significant effect of UVA light compared to the case of SMX, and CAF is not oxidized by PMS alone, thus the reaction conditions might be better approached in the case of CAF degradation.

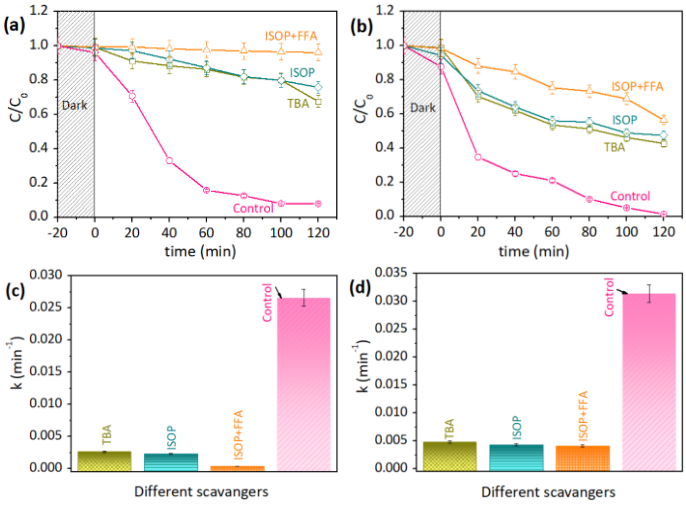

Fig. 3 Degradation data of (a,c) CAF and (b,d) SMX in the presence of different scavengers. Initial concentrations: c_0(CAF) = c_0(SMX) = 50 µM, c($TiNbO_x$) = 0.2 g/L, c_0(TBA) = 10 mM, c_0(ISOP) = 10 mM, c_0(FFA) = 0.5 mM, c_0(PS) = c_0(PMS) = 0.5 mM, at natural pH of distilled water.

Based on these studies, for the degradation of CAF and SMX, 0.2 g L^{-1} of $TiNbO_x$, 0.5 mM PMS, and 50 µM of pollutants at the natural pH of the system were considered as optimal conditions to further investigate PMS activation mechanism and pollutant degradation pathway along with tests in different water matrices. To emphasize the novelty and efficiency of $TiNbO_x$ which was prepared by oxidation of Nb-substitution MXene, a similar synthetic approach was opted to prepare TiO_2 from unsubstituted Ti_2CT_x. The degradation efficiency of this TiO_2 was investigated with and

without PMS under UVA irradiation (Fig. S6) (ESI†). Briefly, only 52 % (k' = 0.0053 min^{-1}) of SMX and 28 % (k' = 0.0026 min^{-1}) of CAF were degraded in the presence of PMS, while a decrease by factor 2 was achieved without PMS. These results clearly revealed that Nb-substitution to the Ti_2CT_x system has a substantial positive role in enhancing the performance of $TiNbO_x$ (see section 3.2).

Identification of ROS reactive intermediates

To investigate the generation and identification of reactive oxygen species (ROS) by the PMS activation in the presence of $TiNbO_x$ under UVA irradiation, scavenging experiments were first performed by employing *t*-butanol (TBA), isopropanol (ISOP) and furfuryl alcohol (FFA). Fig. 3 shows the degradation curves and apparent kinetic constants of CAF and SMX degradation in the presence of TBA, ISOP, and ISOP+FFA (for UVA irradiated systems containing PMS and $TiNbO_x$).

The degradation extents of the pollutants after 2 hours are as follows: 32.5 %, 27.3 %, and 3.9 % for CAF, and 57.3 %, 52.6 %, and 43.6 % for SMX in the presence of TBA, ISOP, and ISOP+FFA, respectively (Fig. 3a and 3b). Similarly, in the presence of TBA, ISOP, and ISOP+FFA, the apparent kinetic constants of the pollutant's degradation decreased by 10, 11.5, and 73.5 times to that of the control experiment for CAF degradation and 6.5, 7.3, and 7.7 times of their control experiment for SMX degradation (Fig. 3c and 3d). Based on the calculations to estimate the contribution of ROS (Text S2) (ESI†), 90.23 % $^{\bullet}OH$, 1.13 % $SO_4^{\bullet-}$, and 7.29 % $^1O_2$ were found to contribute to CAF degradation, thus demonstrating $^{\bullet}OH$ is the major ROS from the activation of PMS. In the case of SMX degradation, a similar trend is observed where the order of ROS contribution is: 84.72 % $^{\bullet}OH$, 1.59 % $SO_4^{\bullet-}$ and 0.64 % $^1O_2$. The summary of the above studies suggested that PMS activation comprises by the formation of $^{\bullet}OH$, $SO_4^{\bullet-}$ and $^1O_2$ species. However, among them $^{\bullet}OH$ is the predominant ROS. Further, the presence of $^{\bullet}OH$ is manifested by using coumarin as a probe and results showed a maximum of 17.3 µM of $^{\bullet}OH$ in 100 minutes (Fig. S7) (ESI†). Moreover, the consumption of PMS by using the spectrophotometric detection method suggested 64% of PMS was consumed during the photocatalytic degradation of caffeine (Fig. S8) (ESI†).[43]

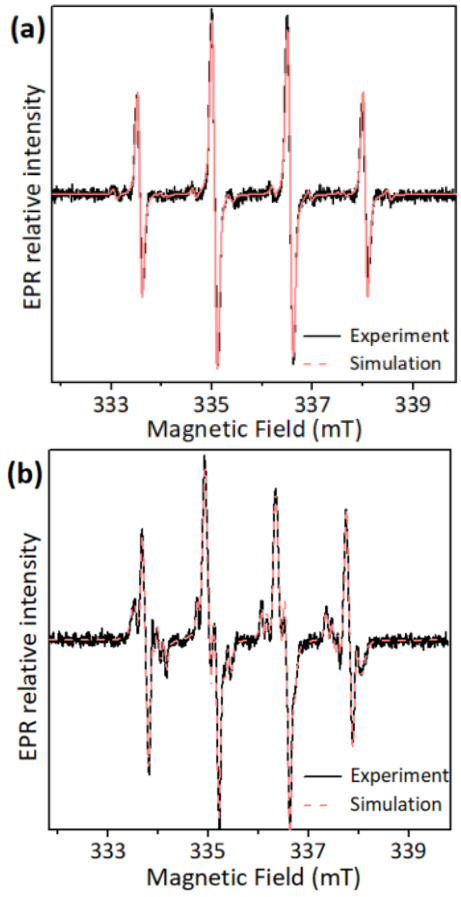

Fig. 4 Experimental and simulated EPR spectra of $TiNbO_x$/SMX/PMS in the presence of (a) DMPO and (b) BMPO spin trap in aerated aqueous suspension measured after UVA exposure (LED@365 nm; radiation dose 6.4 J cm^{-2}). Initial concentrations: $c(TiNbO_x)$ = 0.2 g L^{-1}, c_0(SMX) = c_0(CAF) = 50 µM, c_0(PMS) = 0.5 mM, c_0(DMPO) = 35 mM, c_0(BMPO) = 35 mM.

To provide better insights into the identification of transient paramagnetic species like ROS, the EPR spin trapping technique was employed with 5,5-dimethyl-1-pyrroline *N*-oxide (DMPO) and 5-*tert*-butoxycarbonyl-5-methyl-1-pyrroline *N*-oxide (BMPO) as spin traps.

Table 2 Hyperfine coupling constants and g-values of the DMPO and BMPO spin-adducts elucidated from the simulations of experimental spectra.

Spin-adduct	a_N, mT	a_H^{β}, mT	a_H^{γ}, mT	*g*
$^{\bullet}$DMPO-OH	1.510±0.005	1.466±0.004	–	2.0057
$^{\bullet}$DMPO-SO_4^-	1.317±0.008	1.004±0.006	0.106±0.005, 0.098±0.005	2.0059
$^{\bullet}$DMPO-CR	1.583±0.005	2.298±0.004	–	2.0058
$^{\bullet}$BMPO-OH(I)	1.431±0.005	1.571±0.008	0.065±0.008	2.0058
$^{\bullet}$BMPO-OH(II)	1.413±0.007	1.267±0.005	0.065±0.001	2.0058
$^{\bullet}$BMPO-SO_4^-	1.293±0.010	0.904±0.006	0.134±0.003, 0.083±0.003	2.0059

In systems containing both $TiNbO_x$ and PMS (HSO_5^-), the formation of sulfate radicals from PMS *via* one-electron reduction was expected.[44] Before UVA light exposure, in both reaction systems i.e., aerated aqueous $TiNbO_x$/SMX/PMS and $TiNbO_x$/CAF/PMS dispersion, the •DMPO-OH spin-adduct formation in low concentration (data not shown) was monitored. Upon UVA light exposure (LED@365 nm) the EPR signals significantly increased, and •DMPO-OH (spin Hamiltonian parameters in Table 2, c_{rel} = 94 %) spin-adduct dominated (Fig. 4a). Two other species were monitored in low concentration attributed to •DMPO-SO_4^- (spin Hamiltonian parameters in Table 2, c_{rel} = 2 %) and to •DMPO-CR (spin Hamiltonian parameters in Table 2, c_{rel} = 2 %) spin-adducts. It can be deduced that PMS is reduced at the surface of $TiNbO_x$ to $SO_4^{\bullet-}$ and •OH. The low concentration of •DMPO-SO_4^- could be explained by its fast decomposition to •DMPO-OH (nucleophilic substitution *via* hydrolysis),[45] and $SO_4^{\bullet-}$ can also react with H_2O/HO^- to produce •OH. The spin-adduct •DMPO-CR probably originates from the DMPO cleavage.

Besides the reduction of PMS to $SO_4^{\bullet-}$ and •OH, $TiNbO_x$ may also react with molecular oxygen forming superoxide radical anion ($O_2^{\bullet-}$). Since the spin-adduct •DMPO-O_2^-/OOH is not stable and rapidly disproportionate to •DMPO-OH in water,[46, 47] BMPO spin trap is preferred, due to in aqueous media the •BMPO-O_2^-/OOH has a longer lifetime ($\tau_{½}$ = 23 min) and does not decay into •BMPO-OH. [48, 49] The simulation analysis revealed the presence of three spin-adducts (Fig. 4b), two spin-adducts representing the •BMPO-OH conformers (Table 2: I; c_{rel} = 19 % and II; c_{rel} = 47 %). The presence of these species was expected, and hyperfine coupling constants (*hfcc*) correlate well with previously published data. However, the attribution of the other detected spin-adduct is not so straightforward. The hyperfine coupling constants elucidated from the simulations of experimental spectra (Table 2) do not match to *hfcc* for BMPO superoxide radical anion spin-adducts which were published previously.[48, 49] Therefore, the formation of •BMPO-SO_4^- (Table 2; c_{rel} = 34 %) may be considered. Indeed, to support the assumption, similar experiments were performed under inert atmosphere (removing of the molecular oxygen avoids the generation of $O_2^{\bullet-}$ *via* O_2 reduction). Upon UVA light exposure, the same three spin-adducts were monitored (Fig. S9) (ESI†) corroborating the formation of •BMPO-SO_4^- spin-adduct. Under given experimental condition the stability •BMPO-SO_4^- is longer than its analogue with DMPO, as well as its decomposition to hydroxyl spin-adduct is also suppressed.

Our attention was also oriented toward the detection of singlet oxygen. Oxidation of sterically hindered amines (SHA) results in the formation of stable nitroxide radicals derived from 4(R)-2,2,6,6-tetramethylpiperide *N*-oxyl (R = H–, HO–, O=) which can be detected *via* EPR spectroscopy as characteristic three-line signal.[47] The main species responsible for its oxidation is singlet oxygen, however, interactions with other reactive species cannot be excluded.[50] In the presence of 4-oxo-2,2,6,6-tetramethylpiperide (TMPO), its oxidation to 4-oxo-2,2,6,6-tetramethylpiperide N-oxyl (Tempone) was monitored in aerated $TiNbO_x$/CAF/TMPO and $TiNbO_x$/SMX/TMPO systems under UVA light exposure, but in negligible amounts (Fig. S10a) (ESI†). In water, the lifetime of singlet oxygen is very low ($\tau_{½}$ = 4.2 µs,[46]) thus explaining the weak detection of Tempone under given experimental conditions. In addition, the presence of PMS in the systems caused the immediate formation of a three-line EPR signal with well-resolve ^{13}C-sattelites characteristic for stable nitroxide Tempone (Fig. S10b) (ESI†). This behavior was not expected, however, our observation correlates well with the recently published data,[51] where the mechanism of Tempo generation *via* reaction of SHA with PMS was proposed. For this reason, the detection of singlet oxygen *via* EPR spectroscopy in the system containing PMS and SHA is not reliable.

Proposed mechanism of PMS activation

The degradation of CAF and SMX without the addition of PMS revealed that $TiNbO_x$ is a good photocatalyst. Under UVA irradiation, $TiNbO_x$ triggers the generation of electron/hole pairs (eqn. 3) from which a cascade of consecutive reactions (eqns. 4-8) leads to the formation of ROS as summarized in Fig. 5a. Based on the characterization data (section 3.1) and the literature, $TiNbO_x$ is considered a type-II heterojunction, after homogenization of the Fermi level, composed of TiO_2 and $Ti_2Nb_{10}O_{29}$ thus increasing the lifetime of the charge carriers and leading to high degradation efficiency of CAF and SMX.

$$TiNbO_x \xrightarrow{h\nu} TiNbO_x\ (h_{VB}^+ + e_{CB}^-) \quad (3)$$
$$h_{VB}^+ + HO^- \rightarrow {}^\bullet OH \quad (4)$$
$$e_{CB}^- + O_2 \rightarrow O_2^{\bullet-} \quad (5)$$
$$O_2^{\bullet-} + H^+ \rightarrow HO_2^\bullet \quad (6)$$
$$HO_2^\bullet + HO_2^\bullet \rightarrow H_2O_2 + O_2 \quad (7)$$
$$H_2O_2 \xrightarrow{h\nu} 2\ {}^\bullet OH \quad (8)$$

Besides this, in the presence of PMS (HSO_5^-), further reactive intermediates in higher quantity are produced due to the activation of this radical precursor which took place by the formation of the complex at the surface of $TiNbO_x$ (Fig. 5b).[52] The formation of this surface complex Ti-$OOSO_3^-$ (eqn. 9) is followed by interactions between PMS and $TiNbO_x$, where PMS serves as an electron donor to the conduction band of $TiNbO_x$ (eqn. 10). Simultaneously, HSO_5^- undergoes a reductive conversion to generate $SO_4^{\bullet-}$ and •OH by transfer of electrons through LMCT as shown in eqns. 11 and 12.[52] Also, the photogenerated holes can activate the formation of $SO_5^{\bullet-}$, which can be converted into $SO_4^{\bullet-}$ and •OH (eqns. 13-17).[53, 54]

$$Ti\text{-}OH + HSO_5^- \rightarrow Ti\text{-}OOSO_3^- + H_2O \quad (9)$$
$$Ti\text{-}OOSO_3^- \xrightarrow{h\upsilon} Ti\text{-}{}^\bullet OOSO_3 + e_{CB}^- \quad (10)$$
$$HSO_5^- + e_{CB}^- \rightarrow SO_4^{\bullet-} + HO^- \quad (11)$$
$$HSO_5^- + e_{CB}^- \rightarrow SO_4^{2-} + {}^\bullet OH \quad (12)$$
$$HSO_5^- + h_{VB}^+ \rightarrow SO_5^{\bullet-} + H^+ \quad (13)$$
$$SO_5^{\bullet-} + SO_5^{\bullet-} \rightarrow 2\ SO_4^{\bullet-} + O_2 \quad (14)$$
$$SO_4^{\bullet-} + H_2O \rightarrow {}^\bullet OH + SO_4^{2-} + H^+ \quad (15)$$
$$SO_4^{\bullet-} + HO^- \rightarrow {}^\bullet OH + SO_4^{2-} \quad (16)$$
$$2\ SO_5^{\bullet-} + H_2O \rightarrow 1.5\ {}^1O_2 + 2\ SO_4^{2-} + 2H^+ \quad (17)$$

To support the above-proposed mechanism of PMS activation, the interactions between $TiNbO_x$ and PMS have been investigated by recording XPS spectra before (Text S3) (ESI†), and after the degradation of CAF and SMX in the presence of PMS and $TiNbO_x$ under UVA irradiation (Fig. S11) (ESI†). The peak positions in Ti 2p and Nb 3d spectra remained consistent before and after the degradation experiments with SMX and CAF, suggesting the chemical stability of the catalyst (Fig. S11a, b) (ESI†). After degradation studies, the share of the C-O component at 286.3 eV in the C 1s spectra significantly decreased. A possible explanation is the cleavage of the

O(H) group from C-O(H) bonds which can further support the degradation efficacy. In the O 1s spectra of $TiNbO_x$, the position of the OH component bonded to metallic elements corresponds to the binding energy of around 531.6 eV. However, the position of the OH group can be overlapped with the component corresponding to oxygen defects in the crystal lattice of transition metal oxides.[55]Nonetheless, the same position is overlapped with the main O 1s peak of PMS (Fig. S11c) (ESI†). Thereby, to elucidate the possible attachment of the PMS on the catalyst surface, the K 2p and S 2p spectra of the samples were analyzed (Fig. S11e, f) (ESI†). Presence of sulfur on the surface of $TiNbO_x$ after degradation of SMX and CAF was detected at the same position as for PMS with the main peak around 168.7 eV, which significantly supported the adsorption of PMS on the surface of $TiNbO_x$ (Fig. S11f) (ESI†). Moreover, after the degradation experiment, potassium was also detected on the $TiNbO_x$ surface (Fig. S11e) (ESI†). The position of K 2p lines in PMS spectra is 292.8 eV for K $2p_{3/2}$ and 295.6 eV for K $2p_{1/2}$. However, compared to the PMS spectra the position of K 2p doublet lines of samples after SMX and CAF degradation the position of lines was shifted towards the higher binding energy by 0.2 eV (Fig. S11e) (ESI†).

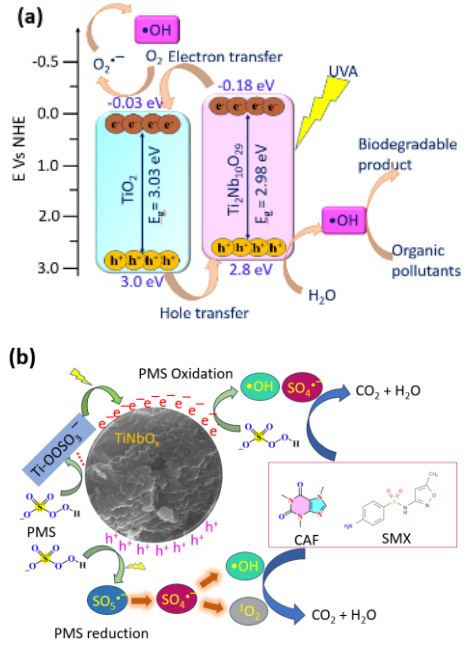

Fig. 5 Schematic representation of pollutant degradation and generation of ROS under UVA irradiation using $TiNbO_x$ photocatalyst (a) without PMS and (b) with PMS.

Speculatively, this effect can be ascribed to charge transfer between the catalyst surface and PMS. Notably, nitrogen which forms SMX and CAF was not detected on the surface of the catalyst after degradation experiments. The presented observations demonstrate the stability of the $TiNbO_x$ after degradation of SMX and CAF. The formation of Ti-$OOSO_3^-$ as a reactive intermediate on the surface of $TiNbO_x$ can enhance the degradation activity via charge transfer from PMS and further support the formation of $SO_4^{\bullet-}$ and •OH as proposed by work.[52]

Proposed degradation mechanism of CAF and SMX

Since the TOC analyses exhibited a mineralization of 69 % and 60 % for CAF and SMX, respectively, the LC-MS was performed to identify the degradation by-products and to provide insights into the degradation mechanism (Fig. 6). For CAF, only hydroxylated caffeine molecule was detected (data not shown), thus suggesting the formation of fragmented by-products such short chain molecules. While caffeine can lead to significant adverse effects at high doses, hydroxylated forms and short-chain metabolites tend to exhibit reduced toxicity and different physiological effects. For SMX, the molecular structure of the degradation by-products was determined from the ion peaks presented in Table S2 (ESI†). SMX was detected at 3.2 min in positive mode with a signal at 254.0588 m/z corresponding to the $[M+H]^+$ and 276.0407 corresponding to the sodium adduct $[M+Na]^+$. In negative mode, SMX was detected at 252.0437 corresponding to $[M-H]^-$. Different reaction mechanisms lead to the formation of by-products. The first degradation pathway involves photoisomerization of the isoxazole ring, resulting in the formation of product P1 which can undergo further oxidation to form the hydroxylated by-product P4. Hydroxylation on the aromatic ring of SMX leads to the formation of product P2 which can subsequently undergo several transformations, including isoxazole ring opening, which produces P10. Additionally, P2 can be further oxidized to yield P8 and di-hydroxylated molecule P3. This di-hydroxylated product can then undergo ring opening reactions, leading to the formation of P11. Other reactions involve the cleavage of the S-N bond in the SMX molecule. This cleavage can produce P5 and P6, highlighting another pathway in the degradation mechanism of SMX. Many of the degradation products (P1 to P11) are expected to exhibit lower toxicity compared to sulfamethoxazole itself, especially those that undergo hydroxylation or ring-opening reactions. P1 to P4, P6, P7, and P11 have been classified as harmful to fish with LC50 values between 10-100 mg/L, while the remaining products were non-harmful (LC50 > 100 mg/L).[56] However specific toxicity data for each degradation product are limited, and further research is needed to fully understand their toxicological profiles.

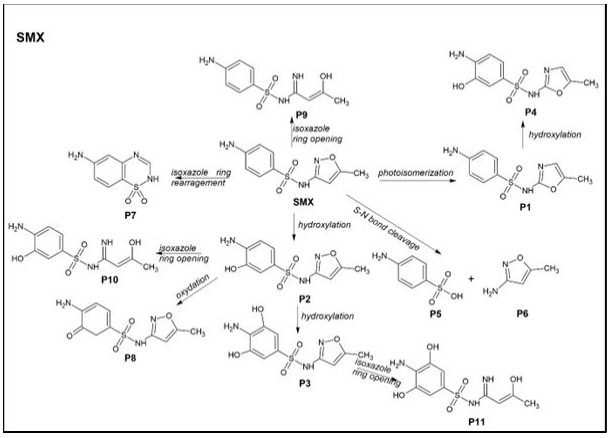

Fig. 6 Degradation pathway of SMX based on the chemical structure of identified products by LC-MS analysis.

Application of $TiNbO_x$/PMS in different water matrices

To estimate the reliability of $TiNbO_x$ for potential integration to WWTP, the degradation of CAF and SMX was performed in tap water and tertiary effluents of WWTP in Bratislava. Indeed, such a technology might aim to be integrated into conventional WWTP in order to achieve higher degradation efficiency to fulfil the requirements of policymakers like the European Commission.[57-60] Under optimal conditions, 49 % (k' = 0.0230 min^{-1}) and 30 % (k' = 0.0181 min^{-1}) of CAF was degraded in tap water (TW) and wastewater (WW), respectively, after 12 h of reaction, whereas for SMX, 68 % (k' = 0.0248 min^{-1}) degradation extent is obtained in TW and 67 % (k' = 0.0203 min^{-1}) in WW (Fig. 7).

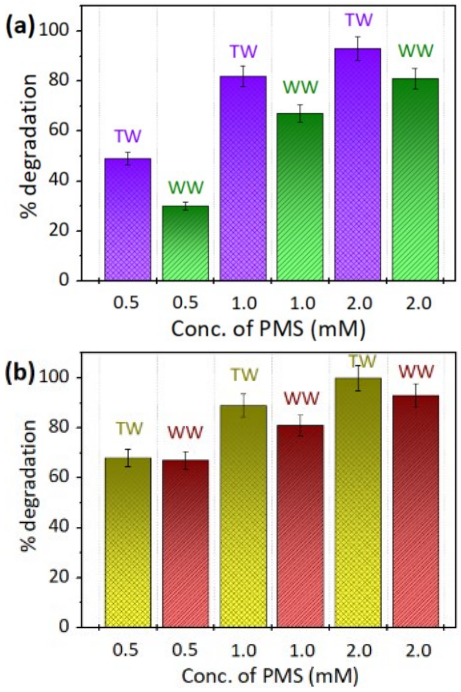

Fig. 7 The degradation extent of (a) CAF and (b) SMX in tap water (TW) and wastewater (WW) by $TiNbO_x$ under UVA with varying PMS concentrations after 12 h. Initial conditions: $c(TiNbO_x)$ = 0.2 g/L, c_0(CAF) = c_0(SMX) = 50 µM.

Since in water matrices, the presence of organic and inorganic compounds can consume PMS or quench the generated ROS, experiments were also performed with higher PMS concentrations (Fig. 7). The degradation extents of CAF and SMX increased with increased PMS concentration and a complete removal was observed in TW for both the pollutants (k' = 0.0302 min^{-1}), whereas 81% (k' = 0.0213 min^{-1}) of CAF and 93% (k' = 0.0270 min^{-1}) of SMX can be degraded in WW. The lower performance of $TiNbO_x$ in CAF and SMX degradation can be explained as (*i*) a variety of suspended and soluble particles can interfere with light utilization by $TiNbO_x$, thus limiting the generation of ROS,[61] and (*ii*) several other organic and inorganic compounds compete with CAF and SMX thus consuming the generated ROS.[9, 62]

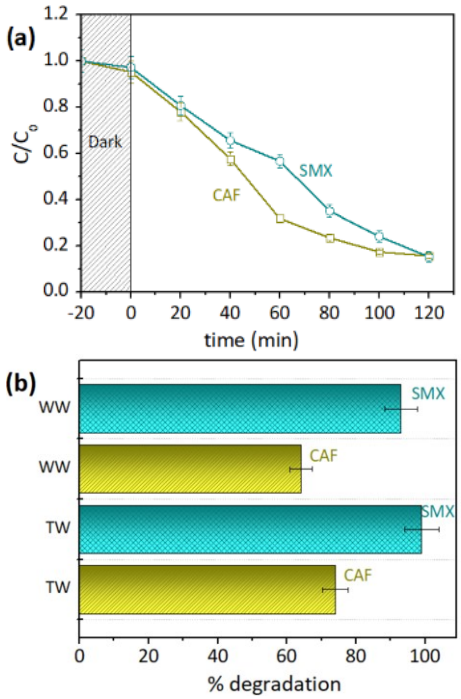

Fig. 8 The degradation response of mixture of CAF and SMX in (a) distilled water by 0.2 g/L of $TiNbO_x$, 0.5 mM of PMS under UVA after 2 h and (b) % degradation of a mixture of CAF and SMX in (b) tap water and wastewater after 12 h, initial conditions: $c(TiNbO_x)$ = 0.2 g/L, c_0(PMS) = 2.0 mM, c_0(CAF) = c_0(SMX) = 50 µM.

Furthermore, the "cocktail" of CAF and SMX was also evaluated in DI water, TP, and WW under optimal conditions. In 120 min, more than 80 % degradation extent (k' = 0.0166 for CAF and 0.153 min^{-1} for SMX) for both pollutants was observed in DI water (Fig. 8a). In a duration of 12 h in TW and WW, SMX degradation has significantly higher efficiency than CAF degradation (Fig. 8b). It can be stated that CAF is more prone to react with $^{\bullet}OH$ than other pollutants.[63] Also, in wastewater matrix effluents, the presence of organic matter which competes with CAF and SMX for the reaction with radical species explains the significant decrease in the degradation efficiency of $TiNbO_x$.[9, 62, 64, 65] However, the obtained results in different water matrices and "cocktail" mode highlight that $TiNbO_x$ can be used as an efficient catalyst for PMS activation, thus opening the door for potential scaling-up studies.

Investigation of reusability behavior

To potentially implement $TiNbO_x$ in a larger-scale reactor, the reusability of $TiNbO_x$ is an important parameter. Fig. 9 shows the performance of $TiNbO_x$ decreased from 98 to 89 % for SMX degradation and from 93 to 78 % for CAF degradation. It should be highlighted the catalyst was reused without any regeneration and minimal mass loss of $TiNbO_x$ during the handling process might occur, thus explaining the decrease in degradation efficiency. Besides, the observed consistency in the peak positions based on XPS and FTIR evidence for the $TiNbO_x$ obtained after CAF and SMX degradation, suggested the chemical surface stability of the catalyst (Fig. S11 and S12) (ESI†).

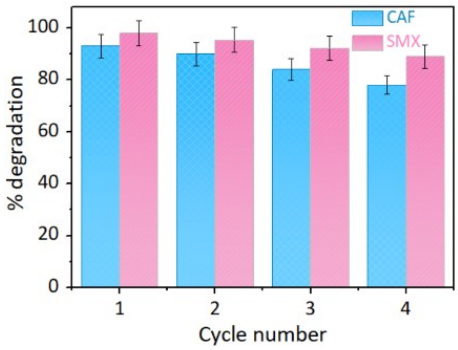

Fig. 9 Reusability behavior of $TiNbO_x$ in the removal of CAF and SMX after 2 h. Initial conditions: $c(TiNbO_x)$ = 0.2 g/L, c_0(PMS) = 0.5 mM, c_0(CAF) = c_0(SMX) = 50 µM.

Experimental

Chemical and reagents

All the chemicals used in this work including metal powders Ti (Alfa Aesar, 99.5 % metal basis, < 44 µm), Nb (Thermo scientific, 99.8 % metal basis, < 44 µm), Al (Thermo scientific, 99.5 % metal basis, < 44 µm), carbon powder (Alfa Aesar, 99 % C, 0.2 % ash, graphite powder, APS-7-11 µm), hydrochloric acid (HCl, Thermo scientific, for analysis, fuming 37 % solution), hydrofluoric acid (HF, ACS reagent, 48 vol.% solution), caffeine (CAF, Merck, anhydrous, 99 %), sulfamethoxazole (Merck, VETRANAL®, analytical standard), *tert*-butanol (TBA, Merck, EMSURE® ACS analysis), isopropanol (ISOP, Merck, LiChrosolv®), furfuryl alcohol (FFA, Sigma Aldrich, analytical standard), potassium peroxymonosulfate (PMS, Sigma Aldrich, OXONE®) and coumarin (Acros organics, > 99 %) were of analytical standard grade and used without further purification. Spin trapping agent 5,5-dimethyl-1-pyrroline *N*-oxide (DMPO) purchased from Sigma-Aldrich was distilled before application, while spin trapping agent 5-*tert*-butoxycarbonyl-5-methyl-1-pyrroline *N*-oxide (BMPO, high purity, Enzo Life Science) was applied as supplied and both spin traps were stored at –18 °C. 4-oxo-2,2,6,6-tetramethylpiperidine (TMPO) was purchased from Sigma-Aldrich.

Preparation of $TiNbO_x$

$TiNbO_x$ was prepared by following earlier established procedure by our group.[66] Briefly, first, $Ti_{1.5}Nb_{0.5}AlC$ (MAX) powders were prepared by mixing metal powders in a stochiometric molar ratio 1.5:0.5:1.2:1.0 (Ti:Nb:Al:C) at 56 rpm for 3 h in the presence of 20 Yttria-stabilized zirconia balls of diameter 10 mm each, using a Turbula T2F mixer. Then, the powders were transferred to an alumina boat and subjected to annealing at 1500 °C for 3 h with a heating rate of 10 °C min^{-1} under a continuous argon (Ar) flow of 0.4 $mLmin^{-1}$.

For the preparation of $(Ti_{0.75}Nb_{0.25})_2CT_x$ (MXene), 1.0 g MAX phase powder was added to a plastic bottle containing 10 mL HF solution and placed in an ice bath to avoid overheating due to exothermic reactions. The mixture was stirred in an oil bath for 72 h at 40 °C. After etching, the solution mixture along with deionized (DI) water was transferred to centrifuge tubes and centrifuged at 3500 rpm for 2 min. The supernatant acid was removed, and the washing procedure (adding DI water, centrifuging, and decanting) was repeated until the pH reached ~ 7. Then, the settled powders in the centrifuge tubes were extracted using DI water, vacuum-filtered, and dried at room temperature.

Finally, 1.0 g of MXene was heated in an alumina crucible with dimensions 100 × 40 × 40 mm in a muffle furnace at 900 °C for 1 h in air, with a heating rate of 5 °C min^{-1}. The obtained white color powder was referred as $TiNbO_x$.

$TiNbO_x$ characterization

The crystal structure of MAX, MXene, and $TiNbO_x$ were examined using X-ray diffractometer (XRD, Rigaku D/Max-2200) equipped with Cu Kα X-ray, at a 2θ step size of 0.02°, a sweep rate of 1° min^{-1}, and operating condition of 40 kV and 40 A. Scanning electron microscopy (SEM) images were recorded using SEM Hitachi S-4800, at 20 kV. Transmission electron microscopy (TEM) examination was performed by using JEOL JEM ARM 200 cF. Fourier Transform Infrared Spectroscopy (FTIR, Ve equipped with rtex 70v, Bruker) with diamond Attenuated total reflectance (ATR) accessory was complementary used for chemical analysis. The surface chemistry was studied by XPS using an AXIS supra spectrometer (Kratos Analytical Ltd., United Kingdom). A monochromatic X-ray Al Kα source (emission current 15 mA, acceleration voltage 15 kV) was used for generating a beam of photons of 1486.6 eV energy. The charging of the samples was compensated using an automatic electron-flood gun system. The core-level spectra were acquired at a pass energy of 20 eV respectively. The pressure in the working chamber was in the order of 10^{-7} Pa. For the analysis of the spectra, CasaXPS software was used.[67] The spectra were referenced using a C 1s signal at 284.8 eV corresponding to C-C, and C-H bonds. The background signal was subtracted by the Shirley algorithm. The specific surface area measurements were carried out using BET (Brunauer-Emmet-Teller method, Sorptomatic 1990 SERIES, Thermo Quest CE Instruments, Italy) in the range of relative pressure p/p_0 = 0.05-0.25, size and adsorption-desorption isotherms were measured at p/p_0 = 0.00 – 1.00, with the low-temperature adsorption method of nitrogen (N_2) at its boiling point of 77.7 K from vacuum to atmospheric pressure. The optical properties of the materials were measured by UV-Vis diffuse reflectance spectroscopy (DRS) using PerkinElmer Lambda-35 with a 50 mm integrating sphere and utilizing $BaSO_4$ as an external reference. The measured reflectance spectra were transformed by the Kubelka-Munk algorithm and Tauc's plot was applied to determine the energy of the band gap (E_g) based on a previous work.[39]

Degradation experiment setups and related analyses

The prepared $TiNbO_x$ was tested for the photocatalytic degradation of caffeine (CAF) and sulfamethoxazole (SMX) under UVA irradiation. The UVA source of irradiation has an intensity of 1.9 mW cm^{-2}.[68] In each case, 0.2 g L^{-1} of $TiNbO_x$ was added to 50 mL solutions of 50 µM CAF and SMX and stirred in the dark for 20 minutes to attain

adsorption-desorption equilibrium. Then, 500 µL aliquots were sampled out every 20 min up to 2 h and filtered out using PTFE microfilter with a pore size of size below 0.45 µm, containing 100 µL of methanol to quench the degradation reaction. The collected samples were analyzed by high-performance liquid chromatography (HPLC, Merck AS-2000 L-6200A L-4250) equipped with a C18 column (Hypersil Gold, 5µm 150 mm × 4.6 mm; Thermo Fisher Scientific). The mobile phase was a mixture of methanol (MeOH) and water (H_2O) using a flow rate of 1 mL min^{-1} in isocratic mode H_2O:MeOH (50:50 v/v). The detection wavelength used for SMX and CAF was 268 nm and 272 nm, respectively. Total organic carbon (TOC) analysis was performed on TOC-5000A (Shimadzu). The degradation kinetic of CAF and SMX were determined by using the pseudo-first-order kinetic.

The effect of reaction conditions on the efficiency of $TiNbO_x$ was examined by varying $TiNbO_x$ and PMS concentrations, and initial pH (from 3 to 9). These studies contributed to determining the optimal conditions for the degradation of CAF and SMX using $TiNbO_x$ in the presence of PMS.

Further, a scavenging study was performed by using *tert*-butanol (TBA), isopropanol (ISOP), and furfuryl alcohol (FFA) to scavenge the generated reactive oxygen species (ROS) during degradation of CAF and SMX under optimized reaction conditions. To find out the suitable concentration of scavengers, the eqn. S4 was used (Text S4) (ESI†),[69] and 10 mM of TBA, 10 mM of IPA, and 0.5 mM of FFA were used. The TBA has high selectivity for •OH with a second-order rate constant of 6.0×10^8 $M^{-1}s^{-1}$, while ISOP could scavenge both •OH and $SO_4^{\bullet-}$ with a rate constant of 8.2×10^7 $M^{-1}s^{-1}$ and 1.9×10^8 $M^{-1}s^{-1}$.[70, 71] Moreover, FFA has capability to quench singlet oxygen ($^1O_2$) with a second-order rate constant of 1.2×10^8 $M^{-1}s^{-1}$,[72] but it can also react with •OH and $SO_4^{\bullet-}$. Therefore, FFA along with ISOP was used to find out the contribution of $^1O_2$.[69]

In addition, indirect technique of electron paramagnetic resonance (EPR) spectroscopy was also used to detect and identify the generated transient paramagnetic intermediates. The dispersions for EPR experiments were prepared in DI water and measurements were carried out at room temperature (295 K) under air employing EPR spectrometer EMX*Plus* (Bruker, Germany) operating at 100 kHz field modulation using the high sensitivity probe-head with the small quartz flat cell (WG 808-Q, Wilmad-LabGlass, optical cell length 0.045 cm). The reaction systems containing $TiNbO_x$ with the other components were prepared directly before measurement and aerated by a gentle airstream before the experiment or saturated by a stream of argon (inert atmosphere). The systems were irradiated at 295 K directly in the EPR high-sensitivity resonator, and the EPR spectra were recorded *in situ*. The value of the UVA irradiance (LED@365 nm), determined using a UVX radiometer (UVP, USA) within the EPR cavity, was 20 mW cm^{-2}. All EPR experiments were performed at least in duplicate. EPR spectra acquisition started 2 minutes after experimental system mixing. The experimental EPR spectra were analysed using WinEPR software (Bruker), while the calculations of spin-Hamiltonian parameters and relative concentrations of individual spin-adducts were performed with the EasySpin toolbox working on the MatLab® platform.[73] To confirm the presence of hydroxyl radicals (•OH), coumarin was used as a probe molecule, since it forms a 7-hydroxycoumarrin compound and further its formation was detected by using fluorescence spectrophotometer (Shimadzu RF-6000) l_{ex}/ le_m = 325 nm/425 nm. All the experiments were repeated three times to obtain a standard deviation in results.

The SMX and CAF degradation products were identified using ultra-high performance liquid chromatography (UHPLC, "Ultimate 3000" ThermoScientific) coupled to high-resolution mass spectrometry equipped with an Q-Exactive Orbitrap. The column was a Phenomenex Kinetex C18 (1.7µm × 100 Å; 100 × 2.1mm) thermostated at 30 °C. The initial gradient was 5% CH_3CN and 95% H_2O with 1% formic acid, followed by a linear gradient to 99% CH_3CN within 8.5 min and kept constant during 1 min. The flow rate was 0.45 mL min^{-1} and the injection volume was 5µL. Ionization was set to 3.2 kV (ESI+) and 3.0 kV (ESI-).

To determine the reusability of $TiNbO_x$ and its potential application in water treatments, additional experiments were performed using tap water and tertiary effluents from municipal WWTP in Bratislava – Petrzalka, Slovakia (collected on 10/10/2023 with physicochemical characteristics presented in Table S3) (ESI†).

Conclusions

For the first time, Nb-substituted binary Ti_2CT_x MXene was used as a precursor to produce an innovative $TiNbO_x$ nano-heterostructure for wastewater treatment. $TiNbO_x$ was investigated as a catalyst for PMS activation in the dark and under UVA irradiation, where it displayed excellent activity in caffeine and sulfamethoxazole degradation. The optimized reaction conditions were found to be 0.2 g L^{-1} of photocatalyst, 0.5 mM of PMS, and 50 µM of pollutants, by examining the effect of pH and PMS concentration under UVA irradiation in 2 h at the natural pH of distilled water.

The study conducted using TBA, ISOP, and FFA as scavengers suggested •OH are the main ROS during the degradation of CAF and SMX. The proposed PMS activation mechanism involves the formation of a surface complex on $TiNbO_x$, which undergoes reductive conversion to generate $SO_4^{\bullet-}$ and •OH, which was supported by EPR spin trapping technique. The degradation pathway of the pollutants suggested several mechanisms including hydroxylation and isoxazole ring-opening reactions. Furthermore, the degradation of CAF and SMX was carried out in water matrices such as tap water and tertiary effluents from WWTP in Bratislava, indicating that $TiNbO_x$ is a promising candidate for potential integration into conventional WWTP.

Author contributions

Shalu Atri: Conceptualization – Investigation – Methodology – Writing: original draft – Writing: review & editing – Funding acquisition
Elham Loni: Investigation – Methodology – Writing: review & editing
Zuzana Dyrcikova: Investigation – Methodology
Frantisek Zazimal: Investigation – Methodology – Writing: review & editing
Maria Caplovicova: Investigation – Methodology

Please do not adjust margins

Dana Dvoranova: Investigation – Methodology – Writing: original draft – Funding acquisition
Gustav Plesch: Conceptualization – Supervision
Miroslava Kabatova: Investigation – Methodology
Marcello Brigante: Investigation – Methodology – Writing: original draft – Funding acquisition.
Michael Naguib: Conceptualization – Supervision – Writing: review & editing – Funding acquisition.
Olivier Monfort: Conceptualization – Supervision – Writing: original draft – Writing: review & editing – Funding acquisition.

Conflicts of interest

There are no conflicts to declare.

Data availability

Data cannot be made available due to legal confidentiality requirements.

Acknowledgements

This work has been carried out in the frame of the PhotoMXene project No. 3305/03/02 co-funded by the EU Horizon 2020 Research and Innovation Program under the Program SASPRO2 COFUND Marie Sklodowska-Curie grant agreement No. 945478. Materials synthesis and characterization at Tulane University was supported by the US National Science Foundation (NSF) CAREER Project DMR-2048164. This work was partially financed by the Slovak Research and Development Agency (SRDA) under the contract No. APVV-21-0039 and VEGA 1/0422/24. This research was also supported by projects LM2023039 and LM2023051 funded by the Ministry of Education, Youth and Sports of the Czech Republic. OM and MB acknowledge Campus France (PHC Stefanik 2023 no. 49871WH) and SRDA under contract No. SK-FR-22-0002 for the financial support of the French-Slovak bilateral project "SOLAREM". OM also acknowledges the Bratislavska Vodarenska Spolocnost (Bratislava Water Company) for supplying effluents to the municipal wastewater treatment plant in Bratislava-Petrzalka along with their routine analytical results. Authors wish to acknowledge Prof. Karol Hensol for their assistance in using fluorescence spectrophotometer.

References

1 S. Castilhos, F.M. de Souza, L.M.S. Colpini, L.M. de Mattos Jorge and O.A.A. Dos Santos, Assessment comparison of commercial TiO_2 and TiO_2 sol-gel on the degradation of caffeine using artificial radiation. *Environ. Sci. Pollut. Res.* 2020, **27**, 22155-22168.

2 R. Luna, C. Solis, N. Ortiz, A. Galicia, F. Sandoval, B. Zermeno and E. Moctezuma, Photocatalytic degradation of caffeine in a solar reactor system. *Int. J. Chem. React. Eng.* 2018, **16**, 1-10.

3 Z. Wu, W. Song, X. Xu, J. Yuan, W. Lv and Y. Yao, High 1T phase and sulfur vacancies in C-MoS_2@ Fe induced by ascorbic acid for synergistically enhanced contaminants degradation. *Sep. Purif. Technol.* 2022, **286**, 120511.

4 P.K. Jjemba, Excretion and ecotoxicity of pharmaceutical and personal care products in the environment. *Ecotoxicol. Environ. Saf.* 2006, **63**, 113-130.

5 A. Karkman, T.T. Do, F. Walsh and M.P. Virta, Antibiotic-resistance genes in wastewater. *Trends Microbiol.* 2018, **26**, 220-228

6 I. Othman, M. Abu Haija, I. Ismail, J.H. Zain and F. Banat, Preparation and catalytic performance of $CuFe_2O_4$ nanoparticles supported on reduced graphene oxide ($CuFe_2O_4$/rGO) for phenol degradation. *Mater. Chem. Phys.* 2019, **238**, 121931.

7 M. Cai, S. Gowrisankaran, M. Gregor, H. Makarov, T. Roch, J. Li, F. Wu, G. Mailhot, M. Brigante and O. Monfort, Unravelling the activation mechanism of oxidants using copper ferrite nanopowder and its application in the treatment of real waters contaminated by phenolic compounds. *Chem. Eng. J.* 2024, **481**, 148623.

8 P. Neta, V. Madhavan, H. Zemel and R.W. Fessenden, Rate constants and mechanism of reaction of sulfate radical anion with aromatic compounds *J. Am. Chem. Soc.* 1977, **99**, 163-164.

9 D. Jia, O. Monfort, K. Hanna, G. Mailhot and M. Brigante, Caffeine degradation using peroxydisulfate and peroxymonosulfate in the presence of Mn_2O_3. Efficiency, reactive species formation and application in sewage treatment plant water. *J. Clean. Prod.* 2021, **328**, 129652.

10 L. Chen, J. Ma, X. Li, J. Zhang, J. Fang, Y. Guan and P. Xie, Strong Enhancement on Fenton Oxidation by Addition of Hydroxylamine to Accelerate the Ferric and Ferrous Iron Cycles. *Environ. Sci. Technol.* 2011, **45**, 3925-3930.

11 Y. Feng, D. Wu, Y. Deng, T. Zhang and K. Shih, Sulfate Radical-Mediated Degradation of Sulfadiazine by $CuFeO_2$ Rhombohedral Crystal-Catalyzed Peroxymonosulfate: Synergistic Effects and Mechanisms. *Environ. Sci. Technol.* 2016, **50**, 3119-3127.

12 Y. Ding, X. Wang, L. Fu, X. Peng, C. Pan, Q. Mao, C. Wang and J. Yan, Nonradicals induced degradation of organic pollutants by peroxydisulfate (PDS) and peroxymonosulfate (PMS): Recent advances and perspective. *Sci. Total Environ.* 2021, **765**, 142794.

13 J. Low, S. Cao, J. Yu and S. Wageh, Two-dimensional layered composite photocatalysts. *ChemComm.* 2014, **50(74)**, 10768-10777.

14 M. Naguib, M. Kortoglu, V. Presser, J. Lu, L. Hultman, J. Niu, M. Heon, Y. Gogotsi and M.W. Barsoum, Two-dimensional nanocrystals produced by exfoliation of Ti_3AlC_2. *Adv. Mater.* 2011, **23**, 4248-4253.

15 Naguib, M., Barsoum, M.W., Gogotsi, Y. Ten years of progress in the synthesis and development of MXenes. *Adv. Mater.* 2021, **33(39)**, 2103393.

16 Y. Sun, X. Meng, Y. Dall'Agnese, C. Dall'Agnese, S. Duan, Y. Gao, G. Chen and X.F. Wang, 2D MXenes as co-catalysts in photocatalysis: synthetic methods. *Nanomicro Lett.* 2019, **11**, 1-22.

17 M., Shekhirev, J., Busa, C.E., Shuck, A., Torres, S., Bagheri, A., Sinitskii and Y. Gogotsi, Ultralarge flakes of $Ti_3C_2T_x$ MXene via soft delamination. *ACS nano* 2022, **16(9)**, 13695-13703

18 Q. Zhang, J. Teng, G. Zou, Q. Peng, Q. Du, T. Jiao and J. Xiang, Efficient phosphate sequestration for water purification by

unique sandwich-like MXene/magnetic iron oxide nanocomposites. *Nanoscale* 2016, **8(13)**, 7085-7093.
19 B. Ahmed, D.H. Anjum, M.N. Hedhili, Y. Gogotsi and H.N. Alshareef, H_2O_2 assisted room temperature oxidation of Ti_2C MXene for Li-ion battery anodes. *Nanoscale* 2016, **8(14)**, 7580-7587.
20 M. Naguib, O. Mashtalir, M.R. Lukatskaya, B. Dyatkin, C. Zhang, V. Presser, Y. Gogotsi and M.W. Barsoum, One-step synthesis of nanocrystalline transition metal oxides on thin sheets of disordered graphitic carbon by oxidation of MXenes. *ChemComm.* 2014, **50(56)**, 7420-7423.
21 C. Zhang, M. Beidaghi, M. Naguib, M.R. Lukatskaya, M.Q. Zhao, B. Dyatkin, K.M. Cook, S.J. Kim, B. Eng, X. Xiao and D. Long, Synthesis and charge storage properties of hierarchical niobium pentoxide/carbon/niobium carbide (MXene) hybrid materials. *Chem. Mater.* 2016, **28(11)**, 3937-3943.
22 S. Husmann, M. Besch, B. Ying, A. Tabassum, M. Naguib and V. Presser, Layered titanium niobium oxides derived from solid-solution Ti–Nb carbides (MXene) as anode materials for Li-ion batteries. *ACS Appl. Energy Mater.* 2022, **5(7)**, 8132-8142.
23 T. Tang, Z. Wang and J. Guan, Electronic structure regulation of single-site MNC electrocatalysts for carbon dioxide reduction. *Acta Phys.-Chim. Sin*. 2022, **39**, 10-3866.
24 Y. Ding, L. Zhu, N. Wang and H. Tang, Sulfate radicals induced degradation of tetrabromobisphenol A with nanoscaled magnetic $CuFe_2O_4$ as a heterogeneous catalyst of peroxymonosulfate. *Appl. Catal. B Environ.* 2013, **129**, 153-162,
25 J. Li, Y. Ren, F. Ji and B. Lai, Heterogeneous catalytic oxidation for the degradation of p-nitrophenol in aqueous solution by persulfate activated with $CuFe_2O_4$ magnetic nano-particles, *Chem. Eng. J.* 2017, **324**, 63-73.
26 P. Yang, A. Shen, Z. Zhu, L. Wang, R. Tang, K. Yang, M. Chen, H. Dai and X. Zhou, Construction of carbon nitride-based heterojunction as photocatalyst for peroxymonosulfate activation: Important role of carbon dots in enhancing photocatalytic activity. *Chem. Eng. J.* 2023, **464**, 142724.
27 S. Irfan, S.B. Khan, M.A.U. Din, F. Dong and D. Chen, Retrospective on Exploring MXene-Based Nanomaterials: Photocatalytic Applications. *Molecules* 2023, **28(6)**, 2495.
28 M. Naguib, O. Mashtalir, J. Carle, V. Presser, J. Lu, L. Hultman, Y. Gogotsi and M.W. Barsoum, Two-dimensional transition metal carbides. *ACS Nano* 2012, **6(2)**, 1322-1331.
29 S. Bhagyaraj, O.S. Oluwafemi, N. Kalarikkal and S. Thomas, eds., Synthesis of inorganic nanomaterials: advances and key technologies 2018.
30 I.J. Badovinac, R. Peter, A. Omerzu, K. Salamon, I. Saric, A. Samarzija, M. Percic, I.K. Piltaver, G. Ambrozic and M. Petravic, Grain size effect on photocatalytic activity of TiO_2 thin films grown by atomic layer deposition. *Thin Solid Films* 2020, **709**, 138215.
31 S. Brunauer, P.H. Emmett and E. Teller, Adsorption of gases in multimolecular layers. *J. Am. Chem. Soc.* 1938, **60(2)**, 309-319.
32 L. Gurvitsch, Physicochemical attractive force. *J. Phys. Chem. Soc. Russ* 1915, **47**, 805-827.
33 G. Horvath and K. Kawazoe, Method for the calculation of effective pore size distribution in molecular sieve carbon. *J. Chem. Eng. Japan* 1983, **16(6)**, 470-475.
34 E.P. Barrett, L.G. Joyner and P.P. Halenda, The determination of pore volume and area distributions in porous substances. I. Computations from nitrogen isotherms. *J. Am. Chem. Soc.* 1951, **73(1)**, 373-380.
35 B.C. Lippens and J.H. De Boer, Studies on pore systems in catalysts: V. The t method. *J. Catal.* 1965, **4(3)**, 319-323.
36 S.A. Kim, S.K. Hussain, M.A. Abbas and J.H. Bang, High-temperature solid-state rutile-to-anatase phase transformation in TiO_2. *J. Solid State Chem.* 2022, **315**, 123510.
37 C. Deng, J. Xu, H. Yu, Y. Liu, X. Cai, H. Yan, L. Fan, M. Shui, L. Yan and J. Shu, One-dimensional $Ti_2Nb_{10}O_{29}$ nanowire for enhanced lithium storage. *Ceram. Inter.* 2022, **48(22)**, 33200-33207.
38 T.Y. Horng, J.A. Davis, K. Fujikawa, N.V. Ganesh, A.V. Demchenko and K.J. Stine, Surface area and pore size characteristics of nanoporous gold subjected to thermal, mechanical, or surface modification studied using gas adsorption isotherms, cyclic voltammetry, thermogravimetric analysis, and scanning electron microscopy. *J. Mater. Chem.* 2012, **22(14)**, 6733-6745.
39 P. Makuła, M. Pacia and W. Macyk, How to correctly determine the band gap energy of modified semiconductor photocatalysts based on UV-Vis spectra. *J. Phys. Chem. Lett.* 2018, **9(23)**, 6814-6817.
40 P. Das, D. Sengupta, U. Kasinadhuni, B. Mondal and K. Mukherjee, Nano-crystalline thin and nano-particulate thick TiO_2 layer: Cost-effective sequential deposition and study on dye-sensitized solar cell characteristics. *Mater. Res. Bull.* 2015, **66**, 32-38.
41 M. Xie, H. Zhu, M. Fang, Z. Huang, Y.G. Liu and X. Wu, Band-gap engineering and comparative investigation of $Ti_2Nb_{10}O_{29}$ photocatalysts obtained by various synthetic routes. *Appl. Surf. Sci.* 2018, **435**, 39-47.
42 E. Lee, H.K. Shon and J. Cho, Role of wetland organic matters as photosensitizer for degradation of micropollutants and metabolites. *J. Hazard. Mater.* 2014, **276**, 1-9.
43 S. Wacławek, K. Grubel and M. Cernik, Simple spectrophotometric determination of monopersulfate. *Spectrochim. Acta A Mol. Biomol. Spectrosc.* 2015, **149**, 928-933.
44 W.D. Oh, Z. Dong and T.T. Lim, Generation of sulfate radical through heterogeneous catalysis for organic contaminants removal: current development, challenges and prospects. *Appl. Catal. B Environ.* 2016, **194**, 169-201.
45 P.L. Zamora and F.A. Villamena, Theoretical and experimental studies of the spin trapping of inorganic radicals by 5, 5-dimethyl-1-pyrroline N-oxide (DMPO). 3. Sulfur dioxide, sulfite, and sulfate radical anions. *J. Phys. Chem. A* 2012, **116(26)**, 7210-7218.
46 S. Feijoo, X. Yu, M. Kamali, L. Appels and R. Dewil, Generation of oxidative radicals by advanced oxidation processes (AOPs) in wastewater treatment: a mechanistic, environmental and economic review. *Rev. Environ. Sci. Bio/Technol.* 2023, **22(1)**, 205-248.
47 Z. Barbierikova, D. Dvoranova and V. Brezova, Application of EPR techniques in the study of photocatalytic systems. In *Material Science in Photocatalysis* 2021, 125-138. Elsevier.
48 A. Misak, V. Brezova, M. Grman, L. Tomasova, M. Chovanec, and K. Ondrias, •BMPO-OOH Spin-Adduct as a Model for Study of Decomposition of Organic Hydroperoxides and the Effects of Sulfide/Selenite Derivatives. An EPR Spin-Trapping Approach. *Antioxidants* 2020, **9(10)**, 918.
49 A. Misak, V. Brezova, M. Chovanec, K. Luspai, M.J. Nasim, M. Grman, L. Tomasova, C. Jacob and K. Ondrias, EPR Study of KO_2 as a Source of Superoxide and (BMPO)-B-center dot-OH/OOH Radical That Cleaves Plasmid DNA and Detects Radical Interaction with H_2S and Se-Derivatives. *Antioxidants* 2021, **10(8)**.
50 Z. Barbierikova, M. Mihalíkova and V. Brezova, Photoinduced oxidation of sterically hindered amines in acetonitrile solutions and titania suspensions (an EPR study). *Photochem. Photobiol.* 2012, **88(6)**, 1442-1454.
51 J.H. Wu, F. Chen, T.H. Yang and H.Q. Yu, Unveiling singlet oxygen spin trapping in catalytic oxidation processes using in

situ kinetic EPR analysis. *Proc. Natl. Acad. Sci.* 2023, **120(30)**, 2305706120.
52 Y. Jo, C. Kim, G.H. Moon, J. Lee, T. An and W. Choi, Activation of peroxymonosulfate on visible light irradiated TiO_2 via a charge transfer complex path. *Chem. Eng. J.* 2018, **346**, 249-257.
53 X.Y. Du, X. Bai, L. Xu, L. Yang and P.K. Jin, Visible-light activation of persulfate by TiO_2/g-C_3N_4 photocatalyst toward efficient degradation of micropollutants. *Chem. Eng. J.* 2020, **384**, 123245.
54 Z. Fang, J. Qi, Y. Xu, Y. Liu, T. Qi, L. Xing, Q. Dai and L. Wang, Promoted generation of singlet oxygen by hollow-shell CoS/g-C_3N_4 catalyst for sulfonamides degradation. *Chem. Eng. J.* 2022, **441**, 136051.
55 M.C. Biesinger, P.P. Brad, W.M.L. Leo, G. Andrea and S.C.S. Roger, X-ray photoelectron spectroscopic chemical state quantification of mixed nickel metal, oxide and hydroxide systems. *Surf. Interface Anal.* 2009, **41(4)**, 324-332.
56 P. Jiang, J. Qiu, Y. Gao, M.I. Stefan and X.F. Li, Nontargeted identification and predicted toxicity of new byproducts generated from UV treatment of water containing micropollutant 2-mercaptobenzothiazole. *Water Res*. 2021, *188*, 116542.
57 European Commission, Off. J. Eur. Union, 2008, **348**, 84-97.
58 European Commission, Off. J. Eur. Union, 2015, **78**, 40-42.
59 European Commission, Off. J. Eur. Union, 2018, **141**, 9-12.
60 European Commission, Off. J. Eur. Union, 2020, **257**, 32-35.
61 J. Liu, Z. Yao, G. Qiu, Y. Wan, W. Song, H. Zeng, F. Yang, D. Zhao, W. Yuan, P. Ju and R. Lin, Generation of reactive oxygen species through dissolved oxygen activation on defected porous carbon for efficient degradation of antibiotics. *Chem. Eng. J.* 2023, **455**, 140602.
62 T.D.D. Oliveira, W.S. Martini, M.D. Santos, M.A.C. Matos and L.L.D. Rocha, Caffeine oxidation in water by Fenton and Fenton-like processes: effects of inorganic anions and ecotoxicological evaluation on aquatic organisms. *J. Braz. Chem. Soc.* 2015, **26**, 178-184.
63 X. Shi, N.S. Dalal and A.C. Jain, Antioxidant behaviour of caffeine: efficient scavenging of hydroxyl radicals. *Food Chem. Toxicol.* 1991, **29(1)**, 1-6.
64 H.L. Liu, Y. Zhang, X.X. Lv, M.S. Cui, K.P. Cui, Z.L. Dai, B. Wang, R. Weerasooriya and X. Chen, Efficient Degradation of Sulfamethoxazole by Diatomite-Supported Hydroxyl-Modified UIO-66 Photocatalyst after Calcination. *Nanomaterials* 2023, **13(24)**, 3116.
65 R. Raj, A. Tripathi, S. Das and M.M. Ghangrekar, Removal of caffeine from wastewater using electrochemical advanced oxidation process: A mini review. *Case Stud. Chem. Environ. Eng.* 2021, **4**, 100129.
66 S. Atri, E. Loni, F. Zazimal, K. Hensel, M. Caplovicova, G. Plesch, X. Lu, R. Nagarajan, M. Naguib and O. Monfort, MXene-Derived Oxide Nanoheterostructures for Photocatalytic Sulfamethoxazole Degradation. *ACS Appl. Nano Mater.* 2024.
67 N. Fairley, V. Fernandez, M. Richard-Plouet, C. Guillot-Deudon, J. Walton, E. Smith, D. Flahaut, M. Greiner, M. Biesinger, S. Tougaard and D. Morgan, Systematic and collaborative approach to problem solving using X-ray photoelectron spectroscopy. *Appl. Surf. Sci. Adv.* 2021, **5**, 100112.
68 S. Gowrisankaran, G.K. Thirunavukkarasu, H. Makarov, T. Roch, G. Plesch, M. Motola, G. Mailhot, M. Brigante and O. Monfort, New insights into the mechanism of coupled photocatalysis and Fenton-based processes using Fe surface-modified TiO_2 nanotube layers: The case study of caffeine degradation. *Catal. Today* 2023, **413**, 114027,
69 Y. Lei, Y. Yu, X. Lei, X. Liang, S. Cheng, G. Ouyang and X. Yang, Assessing the Use of Probes and Quenchers for Understanding the Reactive Species in Advanced Oxidation Processes. *Environ. Sci. Technol.* 2023, **57**, 5433-5444.
70 G.V. Buxton, C.L. Greenstock, W.P. Helman and A.B. Ross, Critical Review of rate constants for reactions of hydrated electrons, hydrogen atoms and hydroxyl radicals ($\cdot OH/\cdot O^-$) in Aqueous Solution. *J. Phys. Chem. Ref. Data* 1988, **17**, 513-886.
71 R.E. Huie, C.L. Clifton and P. Neta, Electron transfer reaction rates and equilibria of the carbonate and sulfate radical anions. *Inter. J. Radiat. Appl. Instrum., Part C Radiat. Phys. Chem.* 1991, **38**, 477-481.
72 X. Mi, P. Wang, S. Xu, L. Su, H. Zhong, H. Wang, Y. Li and S. Zhan, Almost 100 % Peroxymonosulfate Conversion to Singlet Oxygen on Single-Atom CoN_{2+2} Sites. *Angew. Chem.* 2021, **133**, 4638-4643.
73 S. Stoll and A. Schweiger, EasySpin, a comprehensive software package for spectral simulation and analysis in EPR. *J. Magn. Reson.* 2006, **178(1)**, 42-55.